Monthly Notices of the ROYAL ASTRONOMICAL SOCIETY

MNRAS **541,** 1254–1263 (2025) https://doi.org/10.1093/mnras/staf1063
Advance Access publication 2025 July 2

Investigate the GeV gamma-ray emissions from the Perseus molecular cloud

Meng Jiang, Xiao-Na Sun ,★ Qi-Hang Wu, Hai-Ming Zhang, Yun-Feng Liang and En-Wei Liang
Guangxi Key Laboratory for Relativistic Astrophysics, School of Physical Science and Technology, Guangxi University, Nanning 530004, China

Accepted 2025 June 23. Received 2025 June 19; in original form 2025 April 18

ABSTRACT

We study the GeV gamma-ray emissions toward the dense cores IC 348, NGC 1333, and Barnard 1 (B1) with a scale of about 5 pc in the Perseus molecular cloud (MC) using the *Fermi* Large Area Telescope. We reconstruct a background model and find that the column density distribution of molecular hydrogen (H_2) + neutral atomic hydrogen (H I) + dark gas template provides the best-fitting template for spatial analysis, which supports a hadronic origin of the gamma-ray emissions from the dense cores in the Perseus MC. All three cores exhibit hard gamma-ray spectra (photon index ∼2.3), which are consistent with those of young massive star clusters. The gamma-ray spectra of IC 348 and B1 are higher than those derived from the local cosmic rays (CRs), likely originating from inelastic interactions between protons accelerated by massive stellar winds and ambient gas. The gamma-ray spectrum of NGC 1333 exhibits a slight excess above 2 GeV, but a slight deficit below 2 GeV when compared to the spectrum derived from the local CRs. We argue that the suppression of the CR spectrum in NGC 1333 is probably caused by the slow diffusion of CRs, and the distinct characteristic compared to the other two cores may be linked to its nature as a reflection nebula.

Key words: cosmic rays – open clusters and associations: individual: Perseus – gamma-rays: ISM.

1 INTRODUCTION

The Perseus molecular cloud (MC) is one of the nearest star-forming regions to the Sun. Perseus extends from Barnard 5 and IC 348 in the east, through Barnard 3, Barnard 1 (B1) East, and B1 in the centre, to NGC 1333, L1455, L1448 in the west (Bachiller & Cernicharo 1986; Ungerechts & Thaddeus 1987; Bally et al. 2008). IC 348 and NGC 1333 are two identified star clusters in the cloud, and the others are dense cores located in the surrounding areas. Ortiz-León et al. (2018) derive the distance and structure of Perseus by combining trigonometric parallaxes from Very Long Baseline Array observations, estimating the distance to be ∼300 pc with a gradient of about 30 pc across the cloud between the western and eastern edges in the direction of the line of sight, and the distances for IC 348 and NGC 1333 are estimated to be 320 ± 26 and 293 ± 22 pc, respectively. Estimated from visual extinction, the gas mass of Perseus is ∼17 000 $M_\odot$ (Bachiller & Cernicharo 1986). This cloud is associated with the Perseus OB2 association (Bachiller & Cernicharo 1986; Ungerechts & Thaddeus 1987), and a faint ionized hydrogen (H II) region has been detected in this association (Sivan 1974). Wang et al. (2022) collect a sample of 805 previously known young stellar objects (YSOs) in Perseus, with most of the members located in IC 348 and NGC 1333. Additionally, they identify 51 new YSOs and 15 candidates distributed throughout the cloud beyond the two clusters.

IC 348 has been well studied in previous work in the X-ray energy band (Stelzer et al. 2012) and optical/infrared (IR) band (Lada et al. 2006). Luhman, Esplin & Loutrel (2016) compile a membership list for IC 348 and NGC 1333 using optical and near-IR spectroscopy, and infer the age of IC 348 from the ages of these members to be 2–6 Myr. IC 348 includes 478 YSOs (Luhman et al. 2016), with the B5V star BD + 31°643 being the optically brightest and most massive cluster member.

NGC 1333 is the most active region within the cloud for the formation of low- to intermediate-mass stars (Bally et al. 2008; Walawender et al. 2008), and is a complex reflection nebula (Strom, Vrba & Strom 1976). It is estimated to be 1 Myr in age and includes 203 members of YSOs (Luhman et al. 2016). It contains a significant number of embedded protostars, disc stars, Herbig–Haro objects, and molecular outflows (Bally, Devine & Reipurth 1996; Knee & Sandell 2000; Looney, Mundy & Welch 2000; Chini et al. 2001). NGC 1333 is located in the vicinity of three small and dense clumps B1, L1455, and L1448. Of these, B1 is notable for its abundance of molecular gas and the absence of any known population beyond the Class I stage.

Using five years of GeV gamma-ray emissions data from the *Fermi* Large Area Telescope (*Fermi*-LAT), Yang, de Oña Wilhelmi & Aharonian (2014) analyse eight neighbouring MCs, including Perseus. They derive the cosmic rays (CRs) energy spectra and absolute fluxes of the MCs on large scales. For the Perseus region, they find that the derived proton spectrum is comparable to that measured locally by the Payload for Antimatter Matter Exploration and Light -nuclei Astrophysics experiment. Young massive star clusters (YMCs), which predominantly form within dense MCs, have the potential to accelerate CRs, e.g. Cygnus cocoon (Ackermann et al. 2011; Aharonian, Yang & de Oña Wilhelmi 2019; Lhaaso Collaboration 2024), Westerlund 1 (Abramowski et al. 2012), Westerlund 2 (Yang, de Oña Wilhelmi & Aharonian 2018), NGC 3603 (Yang & Aharonian 2017), 30 Dor C (H.E.S.S. Collaboration 2015), RSGC 1 (Katsuta,

★ E-mail: xiaonasun@gxu.edu.cn

Uchiyama & Funk 2017; Sun, Yang & Wang 2020a), W30 (Liu et al. 2019), W40 (Sun et al. 2020b), Mc20 (Sun, Yang & Liang 2022), and NGC 6618 (Liu, Yang & Chen 2022). Interestingly, Yang et al. (2023) report effective shielding of low-energy (<10 GeV) CRs by dense molecular clumps in the Taurus and Perseus clouds.

Here, we re-analyse the GeV gamma-ray emissions near the dense cores of the Perseus region (IC 348, NGC 1333, and B1) to study whether the distribution of CRs exhibits variability on small scales. We investigate the origin of the GeV gamma-ray emissions and the potential acceleration and propagation effects of CRs. In the following Section 2, we investigate the gas and dust distributions around Perseus. In Section 3, we present the details of the analysis of *Fermi*-LAT data and the results. In Section 4, we explore the origin of GeV gamma-ray emissions. We summarize the main conclusions and discuss the propagation and acceleration effects of CRs in Section 5.

2 GAS CONTENT IN THE PERSEUS

The gamma-ray emissions of the Galaxy above $\sim$ 100 MeV are mainly generated from the hadronic interactions between CRs and interstellar gas in dense MCs. As a result, the spatial distribution of gamma-rays should generally follow that of gas. Thus, we first study the spatial distribution of the gas content around the Perseus. We investigate three different gas phases, i.e. molecular hydrogen (H_2), H II, and neutral atomic hydrogen (H I). We also investigate the dust and dark gas distributions.

H_2 is the most abundant molecule in the Universe. Since H_2 does not produce significant absorption or emission lines, it cannot be directly observed. We use the CO data identified by the CO Galactic survey of Dame, Hartmann & Thaddeus (2001) with the 2.6 mm-wave telescope to trace H_2. The relationship between the observed CO intensity and the H_2 column density is employed via a standard method, $N(H_2) = X_{CO} \times W_{CO}$ (Lebrun et al. 1983; Dame et al. 2001), where $N(H_2)$ is the column density of H_2, W_{CO} is the integrated line intensity, and X_{CO} is the H_2/CO conversion factor, which is chosen as 2.0×10^{20} cm^{-2} K^{-1} km^{-1} s as suggested by Dame et al. (2001) and Bolatto, Wolfire & Leroy (2013). The velocity integrated range is $v_{LSR} = [2, 14]$ km s^{-1} (Sun et al. 2007) for IC 348, $v_{LSR} = [-0.75, 14.55]$ km s^{-1} (Bieging, Revelle & Peters 2014) for NGC 1333, and $v_{LSR} = [-1.66, 5.65]$ km s^{-1} (Hirano et al. 1997) for B1. Fig. 1(a) shows the H_2 column density within the velocity range of $v_{LSR} = [-0.75, 14.55]$ km s^{-1}.

The H I column density $N_{H\,I}$ is obtained from the data cube of the H I 4π survey (HI4PI), which is a 21-cm all-sky database of Galactic H I (HI4PI Collaboration 2016). We estimate the H I column density using the equation

$$N_{H\,I} = -1.83 \times 10^{18} T_s \int dv \ln\left(1 - \frac{T_B}{T_s - T_{bg}}\right), \quad (1)$$

where $T_{bg} \approx 2.66$ K is the brightness temperature of the cosmic microwave background radiation at 21 cm. T_B is the brightness temperature of the H I gas, and we truncate T_B to $T_s - 5$ K when $T_B > T_s - 5$ K. T_s is the uniform spin temperature and chosen to be 140 K in the whole Galaxy (Acero et al. 2016a). While in some regions this average T_s is too low, to investigate the effect of the unknown H I optical depth, we derive all $N_{H\,I}$ maps for a sample of uniform spin temperatures (200, 300, 400, 500, 600, 700, and 800 K) (Remy et al. 2017). The derived H I column map with $T_s = 140$ K is shown in Fig. 1(b).

[1]http://simbad.u-strasbg.fr/simbad/

We use the *Planck* free–free map (Planck Collaboration X 2016) to derive the H II column density map, and the conversion factor that transforms the emission measure into the free–free intensity I_ν is chosen from table 1 of Finkbeiner (2003). The column density of the H II is derived using the equation from Sodroski et al. (1997),

$$N_{H\,II} = 1.2 \times 10^{15} \text{ cm}^{-2} \left(\frac{T_e}{1\text{ K}}\right)^{0.35} \left(\frac{\nu}{1\text{ GHz}}\right)^{0.1} \left(\frac{n_e}{1\text{ cm}^{-3}}\right)^{-1} \times \frac{I_\nu}{1\text{ Jy sr}^{-1}}, \quad (2)$$

where T_e represents the electron temperature and is equal to 8000 K, and $\nu = 353$ GHz is the frequency. It is clear from this equation that the H II column density is negatively correlated with the effective density of electrons n_e. We adopt $n_e = 10$ cm^{-3}, which is the value suggested in Sodroski et al. (1997) for the region inside the solar circle. The H II column density map is shown in Fig. 1(c).

When gas and dust are well mixed, the dust column density serves as a reliable proxy for the total gas column density. This capability to trace the 'dark gas' component proves more accurate than traditional tracers like H I and CO. The importance of dust as a comprehensive tracer became clear after the first all-sky IR survey conducted by the *InfraRed Astronomical Satellite*. The dark gas comprises unknown fractions of cold dense H I and CO-free or CO-quiet H_2 (Acero et al. 2016a). According to equation (4) of Planck Collaboration XIX (2011), the total gas column density can be calculated by applying its relation to the dust opacity $\tau_M(\lambda)$:

$$N_H = \tau_M(\lambda) \left[\left(\frac{\tau_D(\lambda)}{N_H}\right)^{\text{dust}}\right]^{-1}, \quad (3)$$

where $\tau_M(\lambda)$ is a function of the wavelength λ. We utilize maps of the thermal dust optical depth at 353 GHz. The ratio $\left(\frac{\tau_D(\lambda)}{N_H}\right)^{\text{dust}} = (1.18 \pm 0.17) \times 10^{26}$ cm^{-2}, as detailed in table 3 of Planck Collaboration XIX (2011), correlates linearly with interstellar hydrogen. We derive the dust column density shown in Fig. 1(d). The dust opacity map lacks velocity information, and thus it is generally impossible to determine the gas content at different distances. However, since Perseus is situated at a relatively high latitude ($b \approx -20°$), there is less interference from other sources in the line-of-sight direction, so we can approximate that most of the observed dust originates from Perseus.

Most of the dust column density correlates well with $N_{H\,I}$ and W_{CO} in the Universe. In the paper Grenier, Casandjian & Terrier (2005), they suggest that the regions of dust that do not correlate with $N_{H\,I}$ and W_{CO}, spatially correlate with excesses in diffuse gamma-ray emissions over expectations from H I and CO, and correspond to the dark gas clouds. To calculate the distribution of dark gas in the Perseus, we follow the method proposed by Grenier et al. (2005). We use the equation $E(B-V)/\tau_{353} = (1.49 \pm 0.03) \times 10^4$ (Planck Collaboration XI 2014) to obtain the dust reddening map, where τ_{353} is the thermal dust optical depth at 353 GHz. We then derive the residual map by subtracting from the dust reddening map those parts that are linearly correlated with $N_{H\,I}$ and W_{CO}.[2] Fig. 2 shows the excess in the residual map of dust reddening $E(B-V)$, which is used to track the dark gas.

[2]This equation shows the best linear fits: $E(B-V) = 1.08 \times 10^{-22} N_{H\,I} + 5.7 \times 10^{-2} W_{CO} + 0.15$. We fit only the data in the Perseus region.

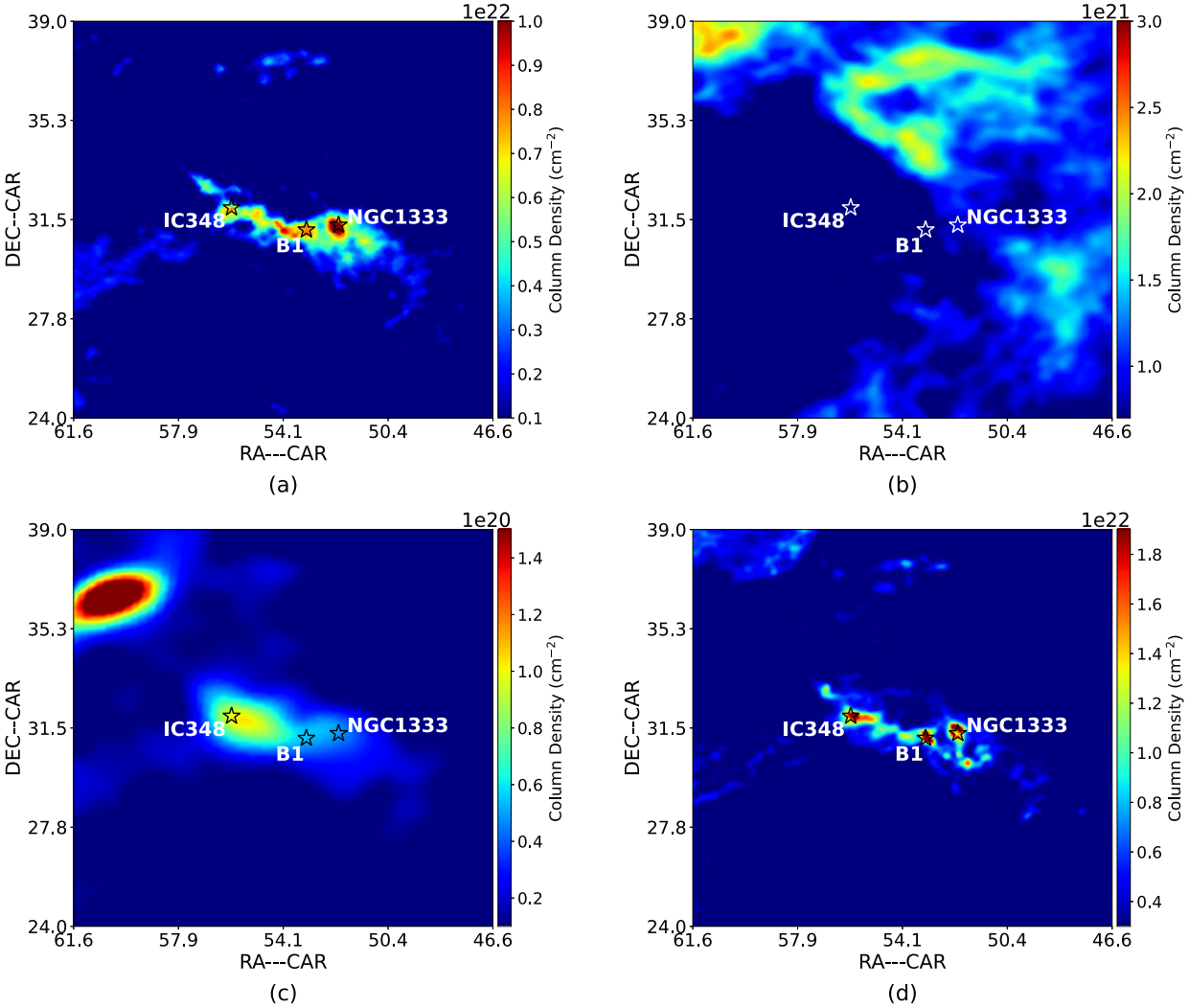

Figure 1. The column density maps of gas and dust. (a) The H_2 map derived from the CO data, (b) the H I map derived from the 21-cm all-sky survey using the uniform spin temperature T_s = 140 K, (c) the H II map derived from the *Planck* free–free map assuming the effective density of electrons $n_e = 10$ cm^{-3}, and (d) the dust map obtained from *Planck* dust opacity map. The pentagrams indicate the positions of the IC 348 (RA = 56.00°, Dec. = 31.97°), NGC 1333 (RA = 52.17°, Dec. = 31.31°), and B1 (RA = 53.32°, Dec. = 31.13°), the coordinates are obtained from the webpage SIMBAD[1], which is the reference database for identification and bibliography of astronomical objects.

The total mass of the cloud within each pixel can be derived from the expression

$$M_{\rm H} = m_{\rm H} N_{\rm H} A_{\rm angular} d^2, \quad (4)$$

where $M_{\rm H}$ is the mass of hydrogen atom, $N_{\rm H}$ is the total column density of the hydrogen atoms per pixel, $A_{\rm angular}$ is the angular area, and d is the distance. We assume that the target regions are spherical in shape and calculate their volumes as $V = \frac{4}{3}\pi r^3$, where r is the radius and is calculated as $r = d \times \theta$(rad), and θ is the observational scale of projection in the sky. The total masses and gas number densities of IC 348, NGC 1333, and B1 are listed in Table 1. The regions selected are those defined in model 1, see Section 3.1 for details. Here, we use $N_{\rm H} = 2N_{\rm H_2} + N_{\rm H\,I}$, and also include the dark gas column density.

3 *FERMI*-LAT DATA ANALYSIS

We select the latest *Fermi*-LAT Pass 8 data from 2008 August 4 (MET 239557417) to 2024 April 14 (MET 737346007), and use the standard LAT analysis software package *v11r5p3*.[3] We choose a 15°×15° region centred on (RA = 54.12°, Dec. = 31.54°) as the region of interest (ROI). Spectral analysis is performed using the *P8R3_SOURCE_V3* version of the post-launch instrument response functions with evclass = 128. We split the data into four event types with associated PSF0 (evtype = 4), PSF1 (evtype = 8), PSF2 (evtype = 16), and PSF3 (evtype = 32), to avoid diluting high-quality events (PSF3) and poorly localized ones (PSF0) to perform a joint likelihood fit for morphology analysis. To reduce the effect of the Earth albedo background, we exclude from the analysis the time intervals when parts of the ROI are observed at zenith angles greater than 90°. In addition, we apply the filter expression (DATA_QUAL >

[3] https://fermi.gsfc.nasa.gov/ssc/data/analysis/software/

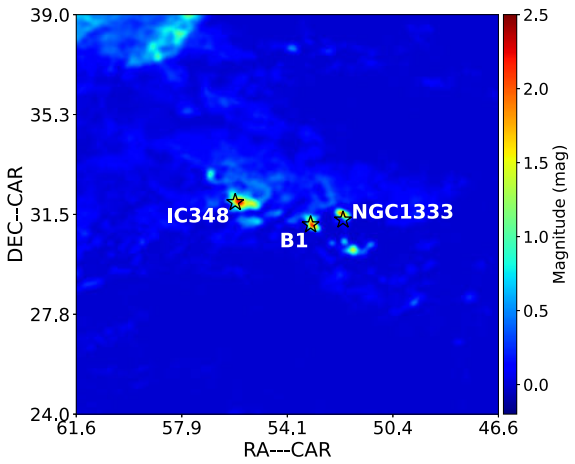

Figure 2. The excess of the dust reddening $E(B-V)$ map over the best linear combination of H I column density and W(CO) intensity maps. The black pentagrams are the positions of the IC 348, NGC 1333, and B1.

Table 1. Total gas masses and number densities within the regions. The tracer consists of H_2 and H I, which includes the component derived by dark gas.

Region	Mass ($10^3 M_\odot$)	Number density (cm^{-3})
IC 348	2.46	2083
NGC 1333	3.51	2090
B1	1.98	2070

0)&&(LAT_CONFIG == 1) to select the data of good time intervals that are not affected by spacecraft events.

We use the script make4FGLxml.py[4] to generate the source model that includes the sources in the *Fermi*-LAT 14-yr catalogue 4FGL-DR4 (Ballet et al. 2023) within the ROI enlarged by 5°, and the parameters for sources with a test statistic (TS) greater than 4 within 10° of the centre are free. For diffuse background components, we use the latest Galactic Interstellar Emission Model (GIEM) *gll_iem_v07.fits* and the isotropic emission model *iso_P8R3_SOURCE_V3_v1.txt*[5] from the *Fermi*-LAT collaboration (Acero et al. 2016b), and we free their normalization parameters. Three point sources (4FGL J0341.9+3153c, 4FGL J0344.2+3203c, and 4FGL J0346.2 + 3235c), which are associated with IC 348, are excluded from the model. We derive the residual map above 300 MeV shown in the left panel of Fig. 3 and find a negative residual in the western area of the MC, around NGC 1333 and B1. It seems that the GIEM provided by the Fermi Collaboration is not suitable for modelling the background since the gamma-ray emissions from the interior of the MC are also included in the GIEM.

We reconstruct the GIEM to improve the background model accuracy. We first employ an IC emission template generated by GALPROP[6] (Vladimirov et al. 2011) tool with the GALDEF identification ${}^{S}Y^{Z}6^{R}30^{T}150^{C}2$ (Acero et al. 2016a), which is utilized in the standard *Fermi*-LAT GIEM, and we set the spectral parameters free. This template features a CR source distribution of pulsars in the Galaxy given by Yusifov & Küçük (2004), a height of the CR propagation halo and radial boundary equal to 6 and 30 kpc, respectively, a uniform spin temperature of 150 K, and the representative diffusive re-acceleration model described in Ackermann et al. (2012). We also generate the dust template from the dust map from Section 2. Since we use the above templates to replace the GIEM, the spectrum of the isotropic component may differ from that of the standard component. We set the spectral parameters of the isotropic emission model *iso_P8R3_SOURCE_V3_v1.txt* free when performing the analysis. As shown in the right panel of Fig. 3, the residual map derived above 300 MeV uses the reconstructed background model. Compared with the residual map on the left panel, this residual map shows significant excess gamma-ray emission in the western area of Perseus (especially at NGC 1333 and B1). In addition, we obtain the column density maps of H_2, H II, and H I in Section 2. As shown in the right panel of Fig. 3, we find that the extended gamma-ray emission has a clear spatial correlation with the distributions of H_2 and dust. In subsequent analysis, we test the templates generated by the gas and dust maps and study the spatial distribution of gamma-ray emissions.

3.1 Morphological analysis

Grenier et al. (2005) and Acero et al. (2016a) report that the template of H I, CO, and dark gas can improve the fit to interstellar gamma-ray emissions compared to the dust template alone. We divide the $2H_2$ + H I + dark gas column density maps, with column densities higher than 1.5×10^{22} cm^{-2} into the IC 348, NGC 1333, and B1 regions, as shown in the white dashed rectangles in Fig. 4. We name the area outside these three regions the 'diffuse' region and simply use the dust map as a template. Due to the limited angular resolution of the *Fermi*-LAT instrument, the gas template size is 5° larger than the ROI. We name this model 'model 1'. We perform the joint likelihood analysis and use the optimizer NEWMINUIT. Since the optimizers included in the Fermitools are known not to work properly for a large number of free parameters above $\sim$ 15,[7] to ensure a robust convergence of likelihood optimization, we fix the parameters of the point sources in the background to their best-fitting values and only free all the parameters of IC 348, NGC 1333, and B1, as well as the normalization parameters of the 'diffuse' components. The likelihood analysis is performed by the *gtlike* tool. To investigate the effect of unknown H I optical depth, we use different H I column density templates derived from several uniform spin temperatures T_s described in Section 2 to fit the observations. The maximum log-likelihood value of the analysis does not exhibit significant changes, thus we still use 140 K for the value of T_s.

We use the $2H_2$ + H I map (model 2) and the dust map (model 3) to create two templates for testing the target regions. The diffuse region still uses the dust template. We perform a joint likelihood analysis. To compare the goodness of fit of different models, we apply the Akaike Information Criterion (AIC, Akaike 1974). AIC is calculated as $-\log(\mathcal{L}) + 2k$, where k is the number of free parameters in the model. We define ΔAIC as $\mathrm{AIC}_{\mathrm{model}} - \mathrm{AIC}_0$, where AIC_0 is the AIC value of model 1 and $\mathrm{AIC}_{\mathrm{model}}$ is that of model 2 or 3. The results from spatial analyses for different models of the target regions are listed in Table 2. We find that model 1 is the best-fitting model.

H II gas could trace massive stars embedded in dense MCs. Liu & Yang (2022) found a hard spectrum diffuse gamma-ray component associated with H II gas in the Galactic plane, which is possibly

[4] https://fermi.gsfc.nasa.gov/ssc/data/analysis/user/
[5] https://fermi.gsfc.nasa.gov/ssc/data/access/lat/BackgroundModels.html
[6] http://galprop.stanford.edu/webrun/
[7] https://root.cern.ch/root/htmldoc/guides/minuit2/Minuit2.html

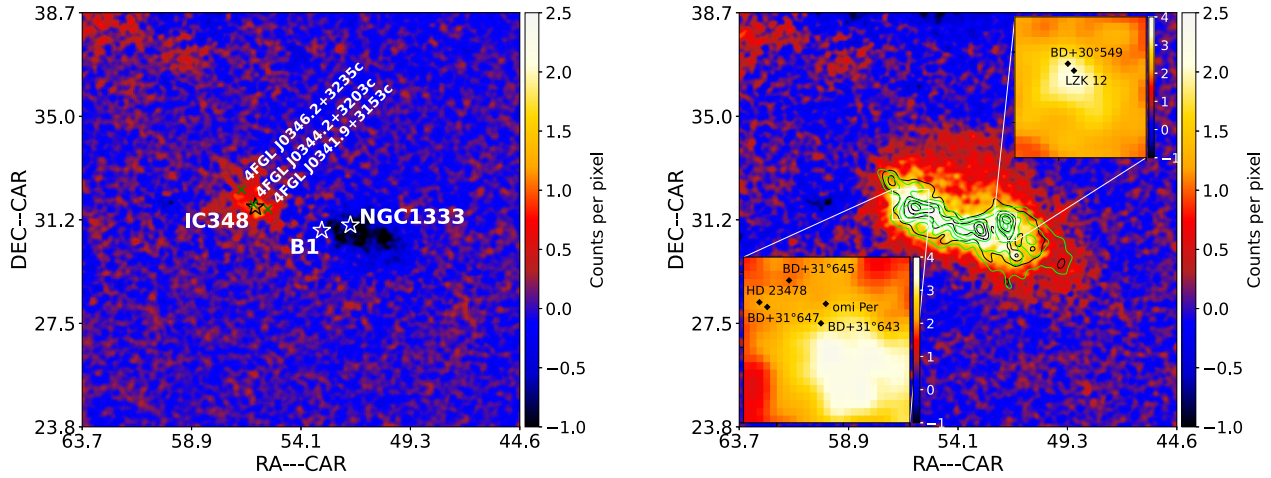

Figure 3. *Fermi*-LAT residual maps are shown after subtracting the background components from 300 MeV to 300 GeV, with a pixel size of 0.05° in the 15° × 15° region around Perseus. The left panel is based on the standard *Fermi* background model. The right panel is based on the reconstructed background model. The pentagrams in the left panel indicate the positions of IC 348, NGC 1333, and B1. The green and black contours in the right panel represent the distributions of H_2 and dust column density as shown in Figs 1(a) and (d). The lower left and the upper right boxes in the right panel show zooms into the boxed area where IC 348 and NGC 1333 are located, with five and two B stars labelled in black diamonds inside. The positions of B stars are obtained from the SIMBAD.

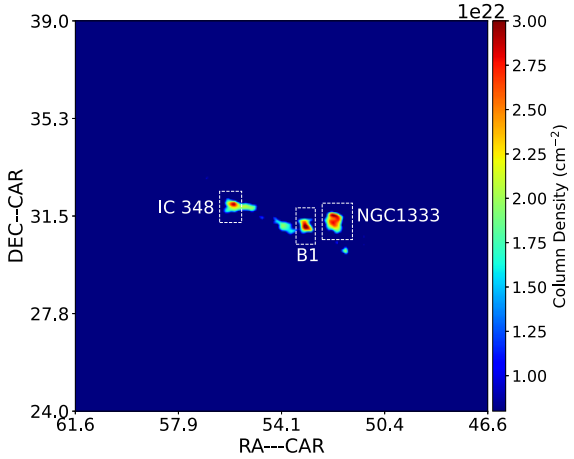

Figure 4. The $2H_2$ + H I + dark gas column density map with the column density above 1.5×10^{22} cm^{-2}, where the white dashed rectangles are the areas of the template for IC 348, NGC 1333, and B1.

Table 2. Spatial analysis results for different models of the target regions at energies above 300 MeV.

Model	$\Delta \log(\mathcal{L})$	D.o.f.	ΔAIC
Model 1 (H I + $2H_2$ + dark gas)	0	17	0
Model 2 (H I + $2H_2$)	−9	17	18
Model 3 (dust)	−15	17	30

associated with CRs accelerated by embedded massive stars (or star clusters). We add the H II component to models 1, 2, and 3 and perform the same analysis. We find that the addition of the H II component has no significant impact on the likelihood value, and the variability of the flux is less than 1 per cent. This may be due to the fact that the H II column density in the target region is one to two orders of magnitude lower than that of the other components.

3.2 Spectral analysis

To determine the spectral shapes of IC 348, NGC 1333, and B1, we perform a likelihood ratio test on the spectral model based on model 1. The significance of the tested model is defined as $\mathrm{TS} = 2\log(\mathcal{L}_{\mathrm{model}}/\mathcal{L}_0)$, where $\mathcal{L}_0$ is the likelihood value of the null hypothesis, for which we set up a power-law (PL) spectral model, and $\mathcal{L}_{\mathrm{model}}$ is the likelihood value of the test models including LogParabola (LogP), PLSuperExpCutoff2 (PLEC), BrokenPowerLaw (BPL). We change the spectral model of one of IC 348, NGC 1333, and B1 while keeping that of the others unchanged. The formulae and corresponding TS values for each spectral type are listed in Table. 3. The spectral shapes of the three regions all favour the LogP model. Above 300 MeV, the gamma-ray emission of IC 348 has photon indices of $\alpha = 2.34 \pm 0.04$, $\beta = 0.06 \pm 0.02$, with an energy flux of $(5.93 \pm 0.23) \times 10^{-12}$ erg cm^{-2} s^{-1}, which corresponds to a gamma-ray luminosity of $\sim 7.27 \times 10^{31}$ erg s^{-1}. Here, a distance of 320 pc is adopted for IC 348. NGC 1333 has photon indices of $\alpha = 2.20 \pm 0.06$, $\beta = 0.12 \pm 0.03$, with an energy flux of $(4.05 \pm 0.23) \times 10^{-12}$ erg cm^{-2} s^{-1}, which corresponds to a gamma-ray luminosity of $\sim 4.16 \times 10^{31}$ erg s^{-1}. The distance for NGC 1333 is adopted as 293 pc. B1 has photon indices of $\alpha = 2.26 \pm 0.06$, $\beta = 0.11 \pm 0.04$, with an energy flux of $(3.90 \pm 0.24) \times 10^{-12}$ erg cm^{-2} s^{-1}, which corresponds to a gamma-ray luminosity of $\sim 4.20 \times 10^{31}$ erg s^{-1}. The distance for B1 is adopted as 300 pc.

3.3 Spectral energy distribution

We extract the spectral energy distributions (SEDs) of IC 348, NGC 1333, and B1 based on model 1. We divide the energy range from 200 MeV to 100 GeV into nine logarithmically space energy bins and use maximum-likelihood analysis to obtain the flux in each energy bin. During the fitting process, we fix the spectral indices and free the normalization parameters in the model. Based on the official *Fermi*

Table 3. Formulae for gamma-ray spectral analysis and likelihood-ratio TS for different spectral types and different regions favoured over a PL null hypothesis.

Name	Formulae	Free parameters	TS (IC 348)	TS (NGC 1333)	TS (B1)
PL	$\frac{dN}{dE} = N_0 \left(\frac{E}{E_0}\right)^{-\Gamma}$	N_0, Γ	–	–	–
LogP	$\frac{dN}{dE} = N_0 \left(\frac{E}{E_b}\right)^{-\Gamma-\beta\log\left(\frac{E}{E_b}\right)}$	N_0, Γ, β	10.40	25.90	13.30
PLEC	$\frac{dN}{dE} = N_0 \left(\frac{E}{E_b}\right)^{-\Gamma} \exp\left(-\left(\frac{E}{E_{\rm cut}}\right)\right)$	$N_0, \Gamma, E_{\rm cut}$	8.54	21.54	11.26
BPL	$\frac{dN}{dE} = \begin{cases} N_0 \left(\frac{E}{E_b}\right)^{-\Gamma_1} & : E < E_b \\ N_0 \left(\frac{E}{E_b}\right)^{-\Gamma_2} & : E > E_b \end{cases}$	$N_0, \Gamma_1, \Gamma_2, E_b$	6.80	12.90	−1.40

website,[8] we use edispbins $= -2$ to calculate the effect of energy dispersion. We calculate 3σ upper limits for energy bins in which the source's significance is below 3σ (TS < 9).

To account for the systematic uncertainty of the IC component generated by GALPROP, we obtain eight IC templates by varying three parameter options in GALPROP, following the approach of Acero et al. (2016b) and Abdollahi et al. (2022), and then repeat their calculations to obtain the systematic uncertainty. The three parameter options are the CR source distributions of supernova remnants according to Case & Bhattacharya (1998) and of pulsars according to Lorimer et al. (2006), the height of the CR propagation halo of 4 and 10 kpc, and the uniform spin temperature of 150 and 10 000 K. In addition, we consider the systematic uncertainty induced by the effective area using the method described on the official *Fermi* website.[9] The total systematic uncertainty is obtained by combining the IC component uncertainty and the effective area uncertainty in quadrature.

The resulting SEDs are shown in Fig. 5. We normalize the gamma-ray emissions to emissivity per H atom. We calculate the number of H atoms based on the masses listed in Table 1. The maximum gamma-ray emission energy in these three regions is up to tens of GeV. The dashed grey lines in Fig. 5 represent the predicted gamma-ray emission spectra of sources, assuming CR densities match those measured locally by AMS-02 (Aguilar et al. 2015). The SED of IC 348 is shown in the left panel, and it is higher than the gamma-ray emission spectrum predicted by local CR. The SED differs from that of Yang et al. (2023) due to the differences in the target model and mass estimation. We find that the SED of NGC 1333 is slightly higher than the local prediction above 2 GeV but lower than the local prediction below 2 GeV, as shown in the middle panel. The SED of B1 is shown in the right panel and is slightly higher than the local prediction.

4 THE ORIGIN OF GAMMA-RAY EMISSIONS

We fit the SEDs using the *Naima* package[10] (Zabalza 2015) to investigate the possible radiation mechanisms of the gamma-ray emissions from IC 348, NGC 1333, and B1. *Naima* allows Marko Chain Monte Carlo fitting using EMCEE (Foreman-Mackey et al. 2013), and it includes a set of models for computing non-thermal radiation from relativistic particle populations as well as a spectral fitting procedure.

Most gamma-ray emissions with energies between 100 MeV and 50 GeV may originate from the pion-decay produced in hadronic collisions when CR protons with energies above 0.5 GeV interact with protons from the interstellar medium (ISM) nuclei through proton–proton (p-p) inelastic interactions (Stecker 1970; Aguilar-Benitez et al. 1991). Through the analyses in Sections 2 and 3, we note that there are clear spatial correlations between the extended gamma-ray emissions of IC 348, NGC 1333, and B1, and the H_2 distribution in the projection on the sky. We assume that the gamma-ray emissions in these regions are produced by p-p inelastic interactions between the accelerated CRs in the dense cores and the ambient gas. The hadronic model based on a PL function of the parent particles can fit the observed data well, as shown by the black lines in Fig. 5. We also test the LogP, ECPL, and BPL for the spectral type of the protons, while there is no significant improvement compared to that of the PL function. For B1, the hadronic model based on the PL spectral type of particles provide the best fit to the observations, except for the first data point in the low-energy band. The corresponding parameters are listed in Table 4. The total energy in all three regions is much lower than that derived from other YMCs. Compared to other systems, these regions host fewer OB stars, which are more dispersed, and the cluster mass is less than 10^4 $M_\odot$. Therefore, it is reasonable to assume that the stellar wind powers in these regions are orders of magnitude lower.

We also consider the leptonic origin of the gamma-ray emissions in the IC scattering scenario. For the photon field of the IC calculations, we consider the cosmic microwave background radiation field, the optical–UV radiation field from star light, and the dust IR radiation field based on the model of Popescu et al. (2017). We use the formalism in Khangulyan, Aharonian & Kelner (2014) with different electron distributions to fit the SEDs. The grey lines in Fig. 5 are the fitting results of the IC model based on the PL model. The corresponding parameters are listed in Table 4. The IC model also provides a good fit to the SEDs, and we cannot formally exclude a leptonic origin for these sources.

5 CONCLUSION AND DISCUSSION

In this work, we report the detection of gamma-ray emissions toward Perseus MC, with detailed analyses of two YMCs, IC 348 and NGC 1333, and a dense core B1 within it. The GIEM provided by *Fermi* is not suitable for background assessment, as gamma-ray emission around NGC 1333 and B1 is included in the GIEM background.

[8] https://fermi.gsfc.nasa.gov/ssc/data/analysis/documentation/Pass8_edisp_usage.html
[9] https://fermi.gsfc.nasa.gov/ssc/data/analysis/scitools/Aeff_Systematics.html
[10] https://naima.readthedocs.io/en/latest/index.html

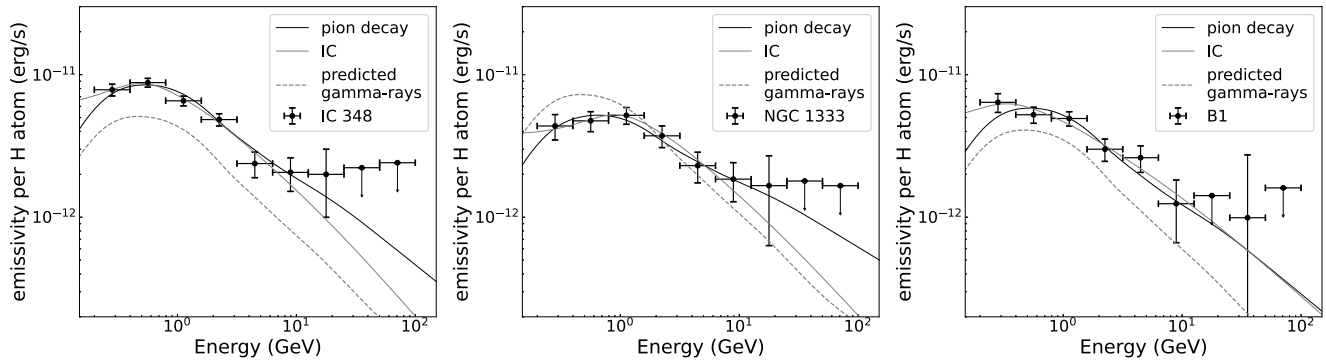

Figure 5. The SEDs of gamma-ray emissions are normalized per H atom above 200 MeV for IC 348 (left), NGC 1333 (centre), and B1 (right). The dashed grey lines show the predicted gamma-ray emissions from the sources, assuming the CR densities match those measured locally by AMS-02. The black and grey lines show the fits for the pion decay and IC models, respectively.

Table 4. SED fitting results for different radiation models (based on the PL model) in different regions.

Region	Model	Index	W_p or W_e (erg) *
IC 348	PP	$2.77^{+0.06}_{-0.06}$	$2.10^{+0.15}_{-0.14} \times 10^{45}$
	IC	$3.92^{+0.13}_{-0.11}$	$1.70^{+0.55}_{-0.39} \times 10^{49}$
NGC 1333	PP	$2.57^{+0.09}_{-0.08}$	$9.84^{+0.99}_{-0.93} \times 10^{45}$
	IC	$3.88^{+0.27}_{-0.22}$	$1.31^{+1.25}_{-0.60} \times 10^{49}$
B1	PP	$2.75^{+0.10}_{-0.09}$	$1.42^{+0.17}_{-0.14} \times 10^{45}$
	IC	$3.70^{+0.14}_{-0.12}$	$6.46^{+2.48}_{-1.64} \times 10^{48}$

Note. * The total energy of the parent protons or electrons (with energy >1 GeV) is required for generating the gamma-ray emission. The fitting uses the hydrogen number density n(H) as listed in Table 1, and distances of 320, 293, and 300 pc for IC 348, NGC 1333, and B1, respectively.

We reconstruct the background using the dust column density map and the IC component generated by the GALPROP. Through spatial analysis, we find that the gamma-ray emissions of these three regions are well modelled by the model generated from H_2, H I, and dark gas. The strong spatial correlations, the characteristic of the SEDs, and the fitting results indicate that the most likely origin of the detected GeV gamma-ray emission is the p-p inelastic interactions of CRs accelerated in the YMCs with the ambient gas, though we also cannot rule out the leptonic scenario.

5.1 IC 348

The spectral shape and spatial extension of gamma-ray emissions associated with IC 348 are similar to those measured in other YMCs. There are about 478 YSOs and five discovered B stars within IC 348, and detailed information is listed in Table 5. We mark the five B stars shown in the right panel of Fig. 3. The positions of these B stars do not coincide with the centre region of the gamma-ray emission and are distributed within a few to tens of pc. We first consider the possibility that CRs are accelerated at the centre. The winds of massive stars may be a suitable site for the acceleration of CRs (Cesarsky & Montmerle 1983; Webb, Axford & Forman 1985; Gupta et al. 2018; Bykov et al. 2020). Morlino et al. (2021) also show that the termination shock formed as a result of the interaction of the intense collective wind of the star cluster with the ISM is a potentially interesting site for particle acceleration. Equation (9) of their work gives the calculation of the position of the termination shock:

Table 5. Detailed information on stars in IC 348, NGC 1333, and B1.

Region	Name	Massive star Type[a]	Total energy[b]	YSO number
IC 348	BD +31°645	B5 E	1.2×10^{49} erg	478[c]
	HD 23 478	B3IV C		
	BD +30°549	B8/9V C		
	omi Per	B1III B		
	BD +31°643	B5 V		
NGC 1333	LZK 12	B5:V + F2: D	9.0×10^{48} erg	203[d]
	BD +30°549	B8/9V C		
B1	–	–	–	∼ 20[e]

Notes. [a] Star types obtained from SIMBAD.
[b] Calculated through Ezoe et al. (2006).
[c] Luhman et al. (2016).
[d] Luhman et al. (2016).
[e] Wang et al. (2022).

$$R_s = 48.6 \dot{M}_{-4}^{3/10} v_8^{1/10} \rho_1^{-3/10} t_{10}^{2/5} \text{ pc}, \quad (5)$$

where $\dot{M}$ is the rate of mass loss due to the collective wind and $\dot{M}_{-4} = \dot{M}/10^{-4}$ $M_\odot$ yr^{-1}, $v_8 = v_W/(1000$ km s$^{-1})$ and v_W is the velocity of expansion of the stellar wind, ρ_1 is the ISM density in the region around the star cluster in units of 1 proton per cm^3, and and t_{10} is the dynamical time in units of 10 Myr. Estimates of the mass-loss rates of O and early B stars range from $\dot{M}_{-4} \sim 10^{-3}$ for O-type stars, to $\dot{M}_{-4} \sim 10^{-5}$–$10^{-4}$ for B0–B3 type stars (Kobulnicky, Chick & Povich 2019). The distances between the B stars within IC 348 are on the order of a few to tens of pc, making it difficult to form a collective stellar wind at such widely dispersed distances. We only consider the stellar wind produced by one B star within IC 348, and we consider $\dot{M}_{-4}$ as 10^{-4}, ρ_1 as 10^3 proton per cm^3, and t as the middle value 4 Myr for the age of IC 348. We calculate that R_s is less than 1 pc. In this equation, they neglect cooling, the actual R_s might be shorter. Therefore, the stellar wind formed by the five observed B stars may hardly accelerate CRs in the centre. In addition, we consider the scenario where CRs are accelerated by the stellar winds of five discovered B stars and then transported to the centre to produce gamma-ray emissions. The specific diffusion process of CRs requires further simulations and calculations.

The dense core and an H II region coincide with the brightest area of the gamma-ray emission. Although no massive stars have been

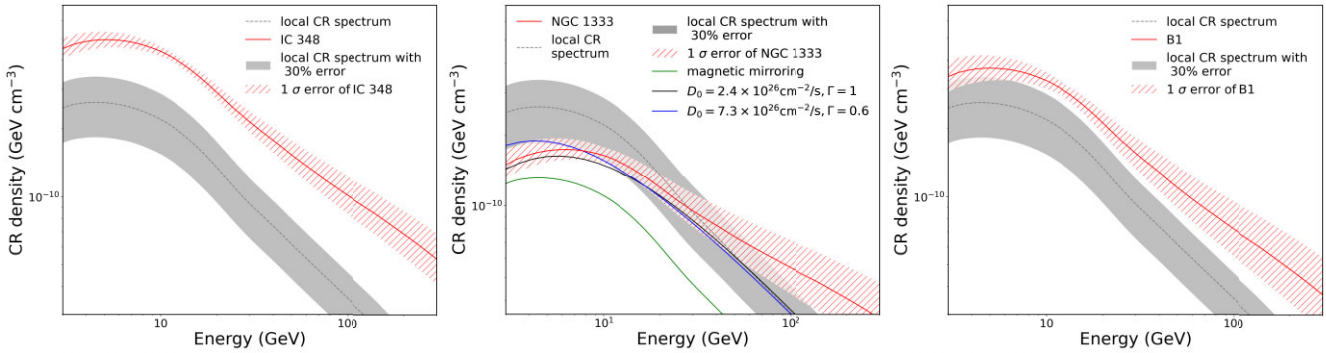

Figure 6. The CR spectra for IC 348, NGC 1333, and B1. The red lines and the shaded red areas represent the CR spectra from the derived proton spectra and those with 1σ errors. The dashed lines and the shaded grey areas represent the predicted local CR spectra and those with 30 per cent errors. In the middle panel, the green line represents the predicted local CR spectra with the effect of magnetic mirroring, and the black and blue lines represent CR spectra in the cloud centre with different values of the diffusion parameter.

detected within it, it cannot be ruled out that they are embedded in the dense core region. We assume that there is an unobserved OB star within the centre region, and that the total kinetic energy supplied by the stellar wind from a single massive star within ∼1 Myr is about 3×10^{48} erg (Ezoe et al. 2006). An OB star can produce a total energy of 1.2×10^{49} erg taking into account the age of the cluster of 4 Myr. The total CR energy we derived based on observation is on the order of 10^{45} erg, much less than that provided by a single OB star. Thus, only one OB star has enough capability to power the CRs here.

There are studies showing evidence of efficient acceleration of CRs in massive protostars (Bosch-Ramon et al. 2010; de Oña Wilhelmi et al. 2023), with outflows that can power the accelerated particles. There are hundreds of YSOs detected in IC 348, and at least one of them is possibly a high-mass protostar in the centre region. We cannot rule out the possibility that the protostars are the source of, or at least contribute to, the observed GeV gamma-ray emissions.

As shown in the left panel of Fig. 5, we can also fit the SED with the IC model. We cannot rule out the leptonic scenario, such as gamma-ray emissions from an unobserved pulsar wind nebula, even though the possibility of there being undiscovered pulsars here is very small.

To account for the impact of the uncertainty of the mass, we adjust the mass of IC 348 to be 30 per cent higher or lower than the estimated value listed in Table. 1. The predicted CR spectrum and its errors are shown as a dashed grey line and a shaded grey area in the left panel of Fig. 6. The CR spectrum derived from the fitted proton spectrum and its 1σ error is shown as the red line and shaded red area. We find that the CR spectrum of IC 348 is still higher than the predicted local CR spectrum. However, a proton spectral index of 2.7 for IC 348 is close to that of the local CR spectrum, and we cannot rule out that these emissions come from the interaction of the CR sea with molecular components.

5.2 NGC 1333

The CR spectrum for NGC 1333, derived from the fitted proton spectrum, and its 1σ error are shown in the red line and shaded red area in the middle panel of Fig. 6. The dashed grey line represents the predicted local CR spectrum. The derived CR spectrum from NGC 1333 shows a deficit in the low-energy range (< 20 GeV) compared to the local CR spectrum on a scale of about 4 pc. We also consider the effect of mass uncertainties on the predicted local CR spectrum, using the same method as for IC 348. This is shown as the shaded grey area. We find that there is still a tentative deficit in the low-energy band within the uncertainties.

We apply the magnetic mirror effect discussed in detail in Owen et al. (2021). The magnetic scaling factor applicable to the CR flux can be defined as $\eta(\chi) = (\chi - \sqrt{\chi^2 - \chi})$ (Desch, Connolly & Srinivasan 2004), where $\chi (\equiv B/B_{\rm ISM})$ is a magnetic concentration parameter, B is the magnetic field strength measured at some location within the MC (including the core region), $B_{\rm ISM}$ is the mean ISM value, and it is generally assumed to be $B_{\rm ISM} \approx 4 - 7\mu$G (Chandrasekhar & Fermi 1953; Zweibel & Heiles 1997). We take $\eta(\chi) = 0.5$ as $\eta(\chi)$ quickly converges to this value when $\chi > 2$. The predicted CR densities are shown by the green line in Fig. 6, indicating that the magnetic mirror effect alone cannot provide a good explanation for the observed CRs in the low-energy band.

Slow CR diffusion in star cluster forming clumps may create a local CR density deficiency (Li & Burkert 2018; Owen et al. 2023). Gas densities associated with clouds may cause strong CR attenuation by hadronic interactions at $>$ GeV energies. Yang et al. (2023) present evidence that diffusive CR propagation persists in MCs, at least to sub-pc clump scales below 10 GeV. To verify whether this hypothesis is consistent with the observations, we describe the propagation of CR using equation (6) of Gabici & Aharonian (2007)

$$\frac{{\rm d}N}{{\rm d}t} = \frac{1}{R^2}\frac{\partial}{\partial R}\left(D(R,E)R^2\frac{\partial N}{\partial R}\right) + \frac{\partial}{\partial E}(\dot{E}N), \quad (6)$$

where N is the particle distribution function of the CRs, R is the distance to the centre of the cloud, and $\dot{E}$ is the energy loss rate of the CR protons. D is the coefficient of diffusion, and we have taken the general form as follows $D(E) = D_0\,({\rm E}/1\ {\rm GeV})^{\Gamma}$, where D_0 is the reference value of the diffusion coefficient at 1 GeV, and Γ is the exponent parameter that characterizes the energy-dependent coefficient. The parameter Γ is influenced by the power spectrum of magnetic field turbulence, which remains highly uncertain. We vary it within physically realistic limits, from 0 (representing energy-independent diffusion) to 1 (indicating Bohm-type diffusion), to determine the value of D_0. The analysis reveals that D_0 falls within the ranges of 2.4×10^{26} cm^{-2} s^{-1} $- 8.0 \times 10^{26}$ cm^{-2} s^{-1} for NGC 1333. The blue and black lines in Fig. 6 show the predicted CR densities for two different values of D_0 and Γ. The value of D_0 at around 1 GeV is about two orders of magnitude smaller than that observed in the ISM. The CR deficit at low-energy band observed in

NGC 1333 requires a slower diffusion, while we cannot rule out the combined effects of slow diffusion and magnetic mirroring.

The proton spectrum above 20 GeV appears harder than the predicted local CR spectrum, implying the existence of a CR acceleration effect within NGC 1333. There are about 203 YSOs and two B stars within NGC 1333, and detailed information is listed in Table 5. We mark the two B stars shown in the right panel of Fig. 3. The two stars, spatially consistent with the gamma-ray emission excess, may accelerate CRs by the termination shocks. Taking a cluster age of 1 Myr into account, two B stars can provide a maximum energy of 9.0×10^{48} erg. The total CR energy we derived based on observation is on the order of 10^{45} erg, which is much lower than the theoretical prediction. The fitting result in the middle panel of Fig. 5 indicates that the leptonic scenario can also fit the observations, although no leptonic sources have been detected in this region.

5.3 B1

The CR spectrum for B1, derived from the fitted proton spectrum, and its 1σ error are shown in the red line and shaded red area in the right panel of Fig. 6. The dashed grey line represents the predicted local CR spectrum. We also find that the CR spectrum of B1 is slightly higher than the local CR spectrum prediction. Unlike IC 348 and NGC 1333, there are no OB stars in B1. Taking into account the very close proximity of B1 to NGC 1333, high-speed stellar winds from NGC 1333 may blow into B1, generating a termination shock to accelerate CRs. Based on equation (5), the position of the termination shock R_s is less than 1 pc if one B star is assumed in NGC 1333. Even though there are two B stars, the collective stellar winds can hardly reach B1. Thus, we can rule out this possibility. There are approximately 20 YSOs in B1, including 10 protostars, all in the Class 0/1 phase. These protostars have outflows but are of low mass ($< 1\,M_\odot$, Hiramatsu, Hirano & Takakuwa 2010). Similarly to IC 348, we cannot confirm whether there are unobserved OB stars, massive protostars, or pulsars in this dense region that accelerate the CRs. We also consider the possibility that CRs are accelerated outside B1 and then propagate into B1 and produce gamma-ray emissions. In this case, it is likely that the accelerated CRs originate from NGC 1333. We consider the effect of mass uncertainties on the local CR spectrum prediction using the same method as for IC 348, the predicted CR spectrum with errors is shown as the shaded grey area in the right panel of Fig. 6. Taking into account the uncertainties, the derived CR densities are still slightly higher than the predicted local CRs. The index of about 2.7 for the proton spectrum of B1 is close to that of the local CR spectrum, and we cannot rule out the possibility that the GeV gamma-ray emissions come from the interactions of the CR sea with molecular components.

The low-energy CR deficit is not observed in IC 348 and B1, while it is detected in NGC 1333. This may be attributed to NGC 1333 being a reflection nebula, which is a kind of passive cloud, and its internal magnetic field and dense material likely affect the propagation of CRs. The specific physical processes require further analysis and discussion.

ACKNOWLEDGEMENTS

This work is supported by National Key R&D Program of China (grant no. 2023YFE0117200), the National Natural Science Foundation of China (NSFC, grant nos 12133003 and 12203022), the Guangxi Talent Program ('Highland of Innovation Talents'), a Science and Technology Program of Guangxi (grant no. 2024GXNSFBA010375). We appreciate the anonymous referee for the instructive comments which help us to improve the paper.

DATA AVAILABILITY

The *Fermi*-LAT data used in this work are publicly available, which is provided online by the NASA-GSFC Fermi Science Support Center.[11] We make use of the CO data[12] to derive the H_2. The data from *Planck* legacy archive[13] are used to derive the H II and dust. The H I data are from the HI4PI.[14]

REFERENCES

Abdollahi S. et al., 2022, ApJ, 933, 204
Abramowski A. et al., 2012, A&A, 537, A114
Acero F. et al., 2016a, ApJS, 223, 26
Acero F. et al., 2016b, ApJS, 224, 8
Ackermann M. et al., 2011, Science, 334, 1103
Ackermann M. et al., 2012, ApJ, 750, 3
Aguilar M. et al., 2015, Phys. Rev. Lett., 114, 171103
Aguilar-Benitez M. et al., 1991, Z. Phys. C, 50, 405
Aharonian F., Yang R., de Oña Wilhelmi E., 2019, Nat. Astron., 3, 561
Akaike H., 1974, IEEE Trans. Autom. Contr., 19, 716
Bachiller R., Cernicharo J., 1986, A&A, 166, 283
Ballet J., Bruel P., Burnett T. H., Lott B., The Fermi-LAT collaboration, 2023, preprint (arXiv:2307.12546)
Bally J., Devine D., Reipurth B., 1996, ApJ, 473, L49
Bally J., Walawender J., Johnstone D., Kirk H., Goodman A., 2008, in Reipurth B., ed., Handbook of Star Forming Regions, Vol. I, The Northern Sky Vol. 4, ASP Monograph Publications, San Francisco, p. 308
Bieging J. H., Revelle M., Peters W. L., 2014, ApJS, 214, 7
Bolatto A. D., Wolfire M., Leroy A. K., 2013, ARA&A, 51, 207
Bosch-Ramon V., Romero G. E., Araudo A. T., Paredes J. M., 2010, A&A, 511, A8
Bykov A. M., Marcowith A., Amato E., Kalyashova M. E., Kruijssen J. M. D., Waxman E., 2020, Space Sci. Rev., 216, 42
Case G. L., Bhattacharya D., 1998, ApJ, 504, 761
Cesarsky C. J., Montmerle T., 1983, Space Sci. Rev., 36, 173
Chandrasekhar S., Fermi E., 1953, ApJ, 118, 113
Chini R., Ward-Thompson D., Kirk J. M., Nielbock M., Reipurth B., Sievers A., 2001, A&A, 369, 155
Dame T. M., Hartmann D., Thaddeus P., 2001, ApJ, 547, 792
de Oña Wilhelmi E., López-Coto R., Su Y., 2023, MNRAS, 523, 105
Desch S. J., Connolly H. C., Jr, Srinivasan G., 2004, ApJ, 602, 528
Ezoe Y., Kokubun M., Makishima K., Sekimoto Y., Matsuzaki K., 2006, ApJ, 638, 860
Finkbeiner D. P., 2003, ApJS, 146, 407
Foreman-Mackey D., Hogg D. W., Lang D., Goodman J., 2013, PASP, 125, 306
Gabici S., Aharonian F. A., 2007, ApJ, 665, L131
Grenier I. A., Casandjian J.-M., Terrier R., 2005, Science, 307, 1292
Gupta S., Nath B. B., Sharma P., Eichler D., 2018, MNRAS, 473, 1537
H.E.S.S. Collaboration, 2015, Science, 347, 406
HI4PI Collaboration, 2016, A&A, 594, A116
Hiramatsu M., Hirano N., Takakuwa S., 2010, ApJ, 712, 778
Hirano N., Kameya O., Mikami H., Umemoto T., Yamamoto S., 1997, ApJ, 478, 631
Katsuta J., Uchiyama Y., Funk S., 2017, ApJ, 839, 129
Khangulyan D., Aharonian F. A., Kelner S. R., 2014, ApJ, 783, 100
Knee L. B. G., Sandell G., 2000, A&A, 361, 671

[11] https://fermi.gsfc.nasa.gov/ssc/data/access/lat/
[12] https://lambda.gsfc.nasa.gov/product/
[13] http://pla.esac.esa.int/pla/#home
[14] http://cdsarc.u-strasbg.fr/viz-bin/qcat?J/A + A/594/A116

Kobulnicky H. A., Chick W. T., Povich M. S., 2019, AJ, 158, 73
Lada C. J. et al., 2006, AJ, 131, 1574
Lebrun F. et al., 1983, ApJ, 274, 231
Lhaaso Collaboration, 2024, Sci. Bull., 69, 449
Li G.-X., Burkert A., 2018, MNRAS, 474, 2167
Liu B., Yang R.-z., 2022, A&A, 659, A101
Liu B., Yang R.-z., Chen Z., 2022, MNRAS, 513, 4747
Liu B., Yang R.-z., Sun X.-n., Aharonian F., Chen Y., 2019, ApJ, 881, 94
Looney L. W., Mundy L. G., Welch W. J., 2000, ApJ, 529, 477
Lorimer D. R. et al., 2006, MNRAS, 372, 777
Luhman K. L., Esplin T. L., Loutrel N. P., 2016, ApJ, 827, 52
Morlino G., Blasi P., Peretti E., Cristofari P., 2021, MNRAS, 504, 6096
Ortiz-León G. N. et al., 2018, ApJ, 865, 73
Owen E. R., On A. Y. L., Lai S.-P., Wu K., 2021, ApJ, 913, 52
Owen E. R., Wu K., Inoue Y., Yang H. Y. K., Mitchell A. M. W., 2023, Galaxies, 11, 86
Planck Collaboration X, 2016, A&A, 594, A10
Planck Collaboration XI, 2014, A&A, 571, A11
Planck Collaboration XIX, 2011, A&A, 536, A19
Popescu C. C., Yang R., Tuffs R. J., Natale G., Rushton M., Aharonian F., 2017, MNRAS, 470, 2539
Remy Q., Grenier I. A., Marshall D. J., Casandjian J. M., 2017, A&A, 601, A78
Sivan J. P., 1974, A&AS, 16, 163
Sodroski T. J., Odegard N., Arendt R. G., Dwek E., Weiland J. L., Hauser M. G., Kelsall T., 1997, ApJ, 480, 173
Stecker F. W., 1970, Ap&SS, 6, 377
Stelzer B., Preibisch T., Alexander F., Mucciarelli P., Flaccomio E., Micela G., Sciortino S., 2012, A&A, 537, A135
Strom S. E., Vrba F. J., Strom K. M., 1976, AJ, 81, 314
Sun K., Kramer C., Mookerjea B., Ossenkopf V., Röllig M., Stutzki J., 2007, 237, 477
Sun X.-N., Yang R.-Z., Liang E.-W., 2022, A&A, 659, A83
Sun X.-N., Yang R.-Z., Liang Y.-F., Peng F.-K., Zhang H.-M., Wang X.-Y., Aharonian F., 2020b, A&A, 639, A80
Sun X.-N., Yang R.-Z., Wang X.-Y., 2020a, MNRAS, 494, 3405
Ungerechts H., Thaddeus P., 1987, ApJS, 63, 645
Vladimirov A. E. et al., 2011, Comput. Phys. Commun., 182, 1156
Walawender J., Bally J., Francesco J. D., Jørgensen J., Getman K.., 2008, in Reipurth B., ed., Handbook of Star Forming Regions, Volume I (monograph 4). Astron. Soc. Pac., San Francisco, p. 346
Wang X.-L., Fang M., Gao Y., Zhang H.-X., Herczeg G. J., Ma H.-J., Chen E., Zhou X.-Y., 2022, ApJ, 936, 23
Webb G. M., Axford W. I., Forman M. A., 1985, ApJ, 298, 684
Yang R.-z., Aharonian F., 2017, A&A, 600, A107
Yang R.-z., de Oña Wilhelmi E., Aharonian F., 2014, A&A, 566, A142
Yang R.-z., de Oña Wilhelmi E., Aharonian F., 2018, A&A, 611, A77
Yang R.-z., Li G.-X., Wilhelmi E. d. O., Cui Y.-D., Liu B., Aharonian F., 2023, Nat. Astron., 7, 351
Yusifov I., Küçük I., 2004, A&A, 422, 545
Zabalza V., 2015, in 34th International Cosmic Ray Conference (ICRC2015). p. 922 (arXiv:1509.03319), doi:
Zweibel E. G., Heiles C., 1997, Nature, 385, 131

This paper has been typeset from a TEX/LATEX file prepared by the author.